Femtosecond laser direct writing of few-mode depressed-cladding waveguide lasers

YUECHEN JIA,[1,2,7] ID RUIYUN HE,[2] JAVIER R. VÁZQUEZ DE ALDANA,[3] HONGLIANG LIU,[4,5] ID AND FENG CHEN[2,6] ID

[1]*INRS-Énergie, Matériaux et Télécommunications, 1650 Blvd Lionel Boulet, Varennes, J3X 1S2 Québec, Canada*
[2]*School of Physics, State Key Laboratory of Crystal Materials, Shandong University, Jinan 250100, China*
[3]*Grupo de Investigación en Aplicaciones del Láser y Fotónica, Universidad de Salamanca, Salamanca 37008, Spain*
[4]*Institute of Modern Optics, Nankai University, Tianjin 300350, China*
[5]*Tianjin Key Laboratory of Optoelectronic Sensor and Sensing Network Technology, Tianjin 300071, China*
[6]*drfchen@sdu.edu.cn*
[7]*yuechen.jia@emt.inrs.ca*

Abstract: We report on mirrorless laser operation of Nd:YVO$_4$ single- and double-cladding waveguides fabricated by femtosecond laser direct writing. Fundamental- (LP_{01}) and high-order-mode (LP_{03}, LP_{05}) guiding and lasing have been observed in waveguides with different geometries and sizes. Double-cladding waveguides exhibit good guiding and lasing performance via inheriting advantages respectively from individual single cladding. As a result, continuous-wave lasing with a threshold as low as 59 mW is obtained, depending on the optical feedback provided only by Fresnel reflections at the waveguide end faces. By using few-layer graphene as saturable absorber, passively Q-switched operation in fabricated waveguides is also achieved.

1. Introduction

Optical waveguides are far more than merely connecting elements between integrated optical components. Benefiting from their strong optical confinement, dielectric waveguides are full of possibilities for functional optical devices as well [1–6]. Solid-state channel waveguide lasers are among the most promising architectures for compact and robust laser sources because they are able to offer enhanced optical gain, reduced lasing threshold, and miniaturized footprints [7–10]. Usually, single-mode waveguides are more favorable with a view to achieving high-power laser output with a high beam quality, especially for Q-switched and mode-locked operations [9,10]. Multimode waveguides, *e.g.* multimode fibers, have recently received renewed attention due to their promising applications such as optical communication [11,12], creation of optical vortices [13,14], optical sensing [15,16], and quantum information technology [17,18]. So far, a lot of efforts has been made to study single-mode waveguides in terms of fabrication, optimization as well as characterization techniques [7–10]. To realize multimode waveguide lasers, the so-called depressed-cladding waveguides (firstly proposed by Okhrimchuk *et al.* in 2005 [19]), which are geometrically analogical to large-mode-area fibers, fabricated by femtosecond laser direct writing (FsLDW) are ideal candidates [10,20,21]. Such tubular cladding waveguides, benefiting from their flexible geometries, sizes and refractive index profiles defined by FsLDW, are capable of supporting excellent single- as well as multi-mode light guiding along all-angle polarizations and offering good lasing performance [10,19–25]. Furthermore, the cross sections of cladding waveguides can be designed to match well to the commercially available fibers, enabling, in principle, optimized connection to construct fiber-waveguide-fiber integrated photonic platforms.
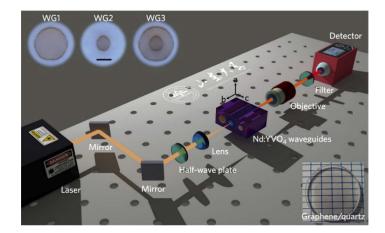
A typical solid-state waveguide laser cavity requires incoupling/outcoupling mirrors, to provide the sufficient optical feedback for laser emission, and probably a modulation element, such as a
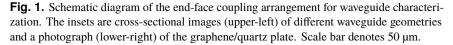
saturable absorber (SA) for Q-switched/mode-locked operation [9,10]. In this way, however, the waveguide laser is never fully monolithic. A more compact design is to use reflective coating on waveguide end facets [10,25,26]. The optical coating can also be even multifunctional, which acts at the same time as a output coupling mirror and a dispersive mirror for mode-locked operation [10,27]. However, designing and transferring desired optical coatings can be a laborious, time consuming and costly effort. Mirrorless waveguide lasers, relying on the high optical gain of waveguide technology by which a Fabry-Perot cavity can be effectively formed simply by the Fresnel reflections, is one of the most straightforward solutions toward reaching the ultimate level of on-chip photonic integration in robust and compact packages. So far, most of the reported mirrorless laser operations of dielectric waveguides are within continuous-wave (CW) regime, realized in liquid phase epitaxy (LPE) grown rare-earth (RE) doped potassium yttrium tungstates ($KY(WO_4)_2$ or KYW), benefitting mainly from the low losses of the fabricated waveguides [28–30]. With a view to achieving low-threshold waveguide lasers, RE-doped yttrium orthovanadate (YVO_4) is actually an ideal alternative due to its high transition cross sections, leading to a high optical gain and a low threshold for CW laser operation [8,31,32].

Depressed-cladding waveguide lasers operating in both CW and pulsed regimes have been realized by FsLDW in Nd:YVO_4 [10,20,33–38]. However, none of these previously reported works use mirrorless waveguide cavity configuration. In this work, for the first time to the best of our knowledge, based on a mirrorless optical cavity configuration, we report on fundamental- (LP_{01}) and high-order-mode (LP_{03}, LP_{05}) guiding as well as lasing (under both CW and Q-switched operations) performance in Nd:YVO_4 single- and double-cladding waveguides fabricated by FsLDW. The double-cladding geometry is similar to the well-known double-clad fibers and has been realized in waveguide lasers to maintain single-transverse mode in the core section [39–41].

2. Waveguide fabrication

The raw Nd:YVO_4 (1 at.% Nd^{3+} ions) crystal wafer used in this work has dimensions of $2(a) \times 7(b) \times 9(c)$ mm^3. All the crystal facets have been well polished to an optical grade. A Ti:Sapphire regenerative amplifier (Spitfire, Spectra Physics), which delivers 795-nm pulses with a temporal duration of 120 fs and a maximum pulse energy of 1 mJ at a repetition rate of 1 kHz, is employed to fabricate cladding structures buried inside the crystal wafer. In the laser-writing process, the incident laser beam is focused through the largest crystal facet (7×9 mm^2) at a maximum depth of 110 µm by a 40× microscope objective (N.A. = 0.65). The crystal wafer is placed on a motorized XYZ micro-positioning stage which allows for precise translation of the sample at a constant velocity (0.5 mm/s in this work to minimize the stress effect induced by laser pulses) with respect to the incident laser beam. A pulse energy of 2 µJ (on sample) is identified as the optimal value in order to produce laser-damage tracks while avoiding crystal cracking. Under our experimental conditions, a damage track with a vertical length of 10 µm and a lateral width of 1.5 µm can be produced via a single scan. A number of parallel scans are performed, with a constant lateral separation of 3 µm, at different depths beneath the crystal surface to define the desired cladding structures: two single-cladding waveguides with radius of 55 (WG1) and 20 µm (WG2), respectively, and one double-cladding waveguide (WG3 with outer and inner radius of 55 and 20 µm, respectively) constructed by two concentric tubular structures that are similar to the single claddings. All the waveguides are written along the *b*-axis (*i.e.* waveguide length of 7 mm in all cases) of the crystal wafer. The end-facets are kept uncoated, as shown in the inset (upper-left) in Fig. 1. The main intention of choosing this FsLDW parameter combination (*i.e.* the combination of waveguide geometry, size and refractive index modification) is realizing efficient guiding and lasing with high-order and fundamental modes in waveguides with large- and small-core areas, respectively.

Fig. 1. Schematic diagram of the end-face coupling arrangement for waveguide characterization. The insets are cross-sectional images (upper-left) of different waveguide geometries and a photograph (lower-right) of the graphene/quartz plate. Scale bar denotes 50 μm.
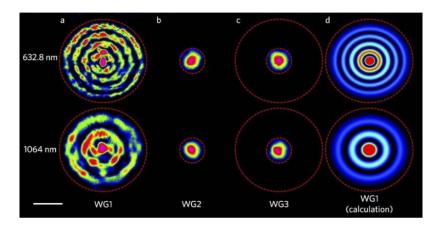
3. Waveguide characterization and laser performance

3.1. Passive regime: waveguide modes and losses

To estimate the optical guiding performance of the fabricated waveguides under passive regime, a standard end-face coupling arrangement is employed, as schematically shown in Fig. 1. The working wavelengths are 632.8 and 1064 nm, where Nd:YVO$_4$ has negligible absorption. A He-Ne laser and a solid-state laser are employed as laser sources, both of which are linearly polarized and are fixed at constant output power during measurements. A half-wave plate is used for rotating the polarization of the incident beam in order to investigate the light guidance along full-angle polarizations. We use a plano-convex lens ($f = 25$ mm, resulting in 20- and 29-μm focal spot sizes at 632.8 and 1064 nm, respectively) and a microscope objective (20×/0.40) for light in- and out-coupling of the sample, respectively.
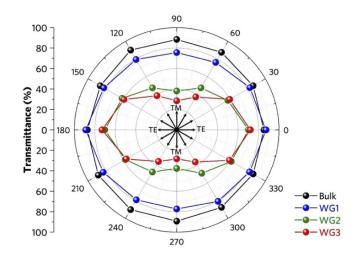
The transmitted waveguide modal profiles are imaged by a CCD camera, as shown in Figs. 2(a)–2(c). As expected, WG1 with large diameter support high-order modes, which have intensity distributions that in analogy to the linearly polarized LP_{05} (at 632.8 nm, shown in upper Fig. 2(a)) and LP_{03} (at 1064 nm, shown in lower Fig. 2(a)) modes in step-index fibers [42]. In fact, the cladding waveguides fabricated in this work have similarities to optical fibers not only in geometries, but also in refractive index distribution, *i.e.* step-index profile. Therefore, we believe it is reasonable to use the formulas that often appear in the context of fiber optics to estimate the refractive index modification caused by FsLDW in this work (although in the fiber case the length is much longer and the ratio between cladding and core areas is usually much larger than that in our case). In step-index fibers/waveguides, the normalized frequency parameter ($V = 2\pi r \cdot NA/\lambda$) determines the number of modes, where λ (632.8 and 1064 nm herein) is the wavelength, r (55 μm for WG1) is the radius of the guide core, and NA is the numerical aperture [42]. By using a Fiber Mode Solver (Matlab code), the required V numbers for effectively supporting LP_{05} and LP_{03} modes as well as the NA values can be easily estimated, resulting in a minimum refractive index modification of $\Delta n = n_{core} - n_{cladding} \approx 3 \times 10^{-4}$ ($n_{core} \approx 1.99/1.96$ is the refractive index of Nd:YVO$_4$ at 632.8/1064 nm). The calculated modal profiles are shown in Fig. 2(d), which fit well to the measured results in Fig. 2(a). The modal profiles in case of WG2 are also checked using the calculated Δn. The fundamental LP_{01} modes at both 632.8 nm and 1064 nm can be determined, which are consistent with the experimental results in Fig. 2(b). Furthermore, based on the Δn, the mode radii of WG2 and WG3 at 1064 nm are calculated to be both around 33.5 μm according

to Marcuse's equation [42], which is in fairly good agreement with the experimental results in Fig. 2. This further strengthens our argument that a step-index profile is a good approximation. In experiments, only the waveguide modes from the inner cladding of WG3 can be detected. This is why the modal profiles of WG3 in Fig. 2(c) are identical to that of WG2 in Fig. 2(b).

Fig. 2. Modal profiles of Nd:YVO$_4$ waveguides: (a) WG1, (b) WG2, (c) WG3, and (d) modelling for WG1, at 632.8 nm (upper figures) and 1064 nm (lower figures). The red dash circles indicate the spatial locations of the FsLDW tracks. Scale bar denotes 50 μm.

Light transmittance performance at 1064 nm is summarized in Fig. 3, which also contains unstructured bulk as reference. The same incoupling lens ($f = 25$ mm) is used for all cases in Fig. 3. Clearly, the light transmittance in the bulk is polarization-independent. This indicates that, in spite of the TE and TM polarization directions in this work correspond respectively to the *c*- and *a*-axis of Nd:YVO$_4$ crystal orientations, the original birefringence has no much impact on the light transmission in this measurement. In contrast to the bulk, however, the maximum transmittance of all the three waveguides occur along TE polarization and the minima along TM polarization. Furthermore, for more compact cladding geometries (WG2 and WG3), the transmittance differences between the maxima (TE) and the minima (TM) are much larger than that of large claddings (WG1). This is most probably induced by the geometrical anisotropy of the laser damage track, resulting in a slight asymmetry of the cladding structures and some residual stress around the waveguide core. This polarization-dependent effect has severe influence on the guiding properties of small-diameter claddings, *e.g.* WG2 and WG3, but very limited impact on large-diameter ones, *e.g.* WG1. The all-angle optical transmission of WG1 is actually very close to that of the bulk. Based on the results in Fig. 2, waveguide losses (including propagation losses and coupling losses) can be obtained, as summarized in Table 1. In our measurements, TE and TM guiding modes have very different losses although very similar modal profiles. We believe this is a solid evidence for the fact that polarization-dependent volume scattering at waveguide boundary (induced by laser damage tracks), rather than mode mismatch, is the main contribution of the total losses estimated in our work. By considering the waveguide losses at 1064 nm (Table 1) and the coupling efficiency formula $\eta_c = \frac{4w_1^2 w_2^2}{(w_1^2 + w_2^2)^2}$ (with w_1 and w_2 are the radii of the incident spot size and guided modes) for single-mode waveguide, the propagation losses of WG2 and WG3 at 1064 nm are determined to be 0.66 and 0.46 dB/cm (with the same coupling loss of 0.44 dB when using the incoupling lens $f = 25$ mm in both cases).

Fig. 3. Polar plot of optical transmittance of Nd:YVO$_4$ waveguides and bulk measured with different polarizations of input light at 1064 nm.

Table 1. Nd:YVO$_4$ waveguide total losses (coupling losses + propagation losses) estimated from Fig. 3

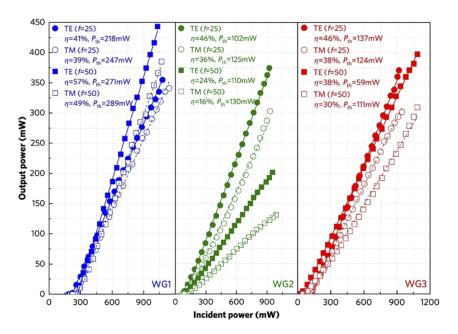|	WG1	WG2	WG3
Loss (TE)	0.08 dB	0.90 dB	0.76 dB
Loss (TM)	0.65 dB	3.71 dB	4.95 dB

3.2. Active regime: CW waveguide laser

In order to investigate the laser performance of the fabricated Nd:YVO$_4$ waveguides, we employed an end-face coupling arrangement similar to that in Fig. 1 but replaced the laser source by a tunable CW Ti:Sapphire laser (Coherent MBR-110) for optical pumping. The pump light is linearly polarized with a wavelength centered at 810 nm. Benefitting from the sufficiently high optical gain provided by the Nd:YVO$_4$ waveguides, a Fabry-Perot cavity can be effectively formed simply by the Fresnel reflections (reflectance of around 11% determined by the refractive index of Nd:YVO$_4$) at waveguide end-facets, which is able to provide sufficient optical feedback for laser oscillation. In the experiments, the laser emission occurs in both forward and backward directions from waveguide end-facets due to the mirrorless configuration. A dichroic mirror is then inserted between the half-wave plate and the incoupling lens to separate the laser output in the backward direction from the pump. The total output power is the sum of laser powers from both directions. We also use incoupling lenses with different focal lengths (f = 25 and 50 mm, resulting in focal spot sizes of 23 and 46 µm, respectively) to investigate how the coupling efficiency influences the lasing performance. The same microscope objective (20×/0.40) is used for outcoupling in all cases. The alignment in each measurement is separately optimized for reaching maximum output power.
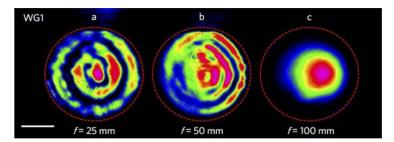
The input-output dependences are shown in Fig. 4. The exact lasing thresholds P_{th} and slope efficiencies η are also indicated separately for each waveguide. The central lasing wavelength is 1065 nm with the full wave at half maximum (FWHM) value of 0.5 nm (with a spectrometer resolution of 0.2 nm), corresponding to the transition band $^4F_{3/2} \rightarrow {}^4I_{11/2}$ of Nd^{3+}. The laser output is linearly polarized with $E \| c$, which is naturally selected by the anisotropy of the gain [43]. From the seemingly miscellaneous data points in Fig. 4 four key features of Nd:YVO$_4$ cladding waveguide lasers can be summarized:

a All the waveguides show slightly superior lasing performance (higher slope efficiencies, lower lasing thresholds as well as larger maximum output power) under optical pump with TE, with respect to TM, polarization. This we believe, according to the modified Caird analysis [44], is mainly caused by the higher waveguide losses along TM polarization, as verified in passive regime (in Fig. 3 and Table 1).

b As expected, the more compact the active waveguide core is, the lower lasing threshold it possesses. As a result, WG2 (>102 mW) gives only half of WG1's (>218 mW) lasing threshold. For a comparison, the CW laser operation when moving the pump beam into the bulk area (the least compact geometry) is also tested. Based on the same optical setup and mirrorless cavity, a lasing threshold around 300-400 mW with very unstable laser output power is obtained. This result further demonstrates the advantages of compact waveguide geometries in terms of constructing low-threshold lasers.

c Large-cladding waveguide (WG1) laser shows less sensitivity on the incoupling condition compared to that of WG2. The focal spot diameters for different incoupling lenses are different, giving dissimilar modal mismatch, *i.e.* coupling efficiency, between the pump and the waveguide mode. However, this modal mismatch has relatively little impact (with <20% difference on maximum output power) on WG1 due to its large diameter. While for WG2, the difference on maximum output power is >40%. In fact, all the laser modes of WG2 and WG3 are very similar to that measured in passive regime (results at 1064 nm in Fig. 2), even using different incoupling lenses. However, for WG1, the laser mode varies, as shown in Fig. 5. In case of $f = 25$ mm (23-μm spot size), the intensity distribution in Fig. 5(a) is identical to that in Fig. 2(a), *i.e.* LP_{03} mode. For $f = 50$ mm (46-μm spot size), the LP_{03} mode gets weakly coupled, as shown in Fig. 5(b), showing a kind of hybrid modal profile composed of LP_{03} and lower-order mode. For comparison, we also use a lens with $f = 100$ mm (92-μm focal spot size) for incoupling. In such a case, only a fundamental mode with reduced mode size can be excited, as shown in Fig. 5(c). These results prove that, first, large-cladding waveguide is able to support multimode lasing with little impact on the laser output and efficiency (the laser performance of WG1 in case of $f = 100$ mm is not shown, but it is quite similar to that in Fig. 4) simply by adjusting the coupling condition; second, a suitable incoupling condition is highly required for achieving an efficient high-order-mode waveguide lasing.

d Double-cladding waveguide (WG3) combines the respective advantages from large- and small-cladding waveguides via its outer- and inner-cladding, giving fundamental-mode lasing with low lasing threshold and meanwhile low sensitivity on coupling efficiency. Notably, a lasing threshold as low as $P_{th} = 59$ mW has been obtained in case of WG3 when using TE-polarized pump and incoupling lens with $f = 50$ mm, relying only on the non-coated waveguide end-facets. It is noteworthy that our calculation of incident pump power here does not take into account the waveguide coupling losses. By considering the waveguide losses as described in Section 3.1 and the coupling efficiency for pump spot size of 46 μm, a lasing threshold of $P_{th} <50$ mW can be expected for WG3.

The maximum output power from WG3 is approximately 397 mW, which is lower than that of WG1 (443 mW) but slightly higher than that of WG2 (374 mW). Since the waveguide loss of WG3 is much higher than that of WG1, there is still great room for improvement to get better lasing performance from double-cladding waveguides. The highest slope efficiency of WG3 is 46%, which is equivalent to that of WG2 but slightly lower than that of WG1 (57%).

Fig. 4. Output power as a function of incident power obtained from Nd:YVO$_4$ cladding waveguides (left: WG1, middle: WG2, right: WG3) for TE (filled markers) and TM (open markers) polarized pump, respectively, employing incoupling lenses with focal lengths of 25 (circles) and 50 mm (cubes). Solid and dashed lines are linear fit of the experimental data.
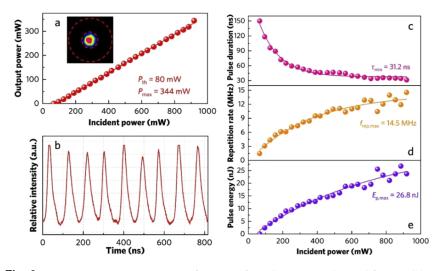

Fig. 5. Laser modes at 1.06 μm of WG1 when using incoupling lens with different focal lengths: (a) $f = 25$ mm, (b) $f = 50$ mm, and (c) $f = 100$ mm.

3.3. Active regime: Q-switched waveguide laser

To further explore the lasing performance operating at pulsed regime (passive Q-switching) of the fabricated waveguides, we used a graphene thin film (~5 layers grown by chemical vapor deposition) coated quartz plate (2-mm thick) as SA, as shown in the lower-right inset in Fig. 1. The SA is adhered to the output facet of the waveguide, serving as an output coupler (OC, with single-pass transmittance of around 80% at 1.06 μm) in parallel. The end-face coupling arrangement is remained the same as that for CW laser operation. The Q-switched lasing performance of WG3 is measured using pump with TE polarization and an incoupling lens with $f = 25$ mm, results are summarized in Fig. 6. The central wavelength is 1065.2 nm. Comparing the results in Fig. 6(a) (in case of TE pump and $f = 25$ mm for WG3) to that in Fig. 4, we find that adhering a SA to the waveguide end-facet results in a slightly reduced lasing threshold (80 mW compared to 137 mW) and lower maximum output power (344 mW compared to 370 mW, giving a Q-switching conversion efficiency of >90%). This is mainly because the SA we

used here is also serving as an OC, providing a slightly lower transmittance (a total of 71% considering Fresnel reflection) than Fresnel transmission (89% transmittance) given only by the bare waveguide end facet. The laser mode shown in the inset of Fig. 6(a) is identical to that in the passive regime in Fig. 2(c). A typical oscilloscope trace of the Q-switched pulse train (at repetition rate of 7.1 MHz) of WG3 is shown in Fig. 6(b). The Q-switching intensity instabilities of <15% can be attributed to the SA heating due to the non-absorbed pump power. The key parameters, namely temporal duration (τ), repetition rate (f_{rep}) and single pulse energy (E_p), of the generated laser pulses are also determined, as summarized in Figs. 6(c)–6(e). By increasing the pump power, the pulse duration decreases from 150 ns to 31.2 ns (Fig. 6(c)), whilst the repetition rate increases from 1.5 MHz to 150 MHz (Fig. 6(d)), resulting in a maximum single pulse energy of 26.8 nJ (Fig. 6(e)). Such a dependence between the τ (f_{rep}) and the pump power is typically observed in lasers passively Q-switched by fast SAs and is related to the dependence of SA bleaching on the pump power [45].

Fig. 6. (a) Average output power as a function of incident power obtained from WG3 in Q-switched regime. The inset shows the laser mode. The red dash circles indicate the spatial locations of the FsLDW tracks. (b) Oscilloscope trace of the Q-switched pulse train at repetition rate of 7.1 MHz. The (c) pulse duration, (d) repetition rate and (e) single pulse energy of the delivered pulses as a function of the incident pump power.

4. Summary

In conclusion, we have fabricated low-loss Nd:YVO$_4$ cladding waveguides supporting fundamental and high-order modes by FsLDW. Based on a mirrorless cavity configuration, efficient CW and Q-switched laser operations have been achieved, resulting in a lasing threshold as low as 59 mW (WG3), a slope efficiency as high as 57% (WG1), and a maximum output power as large as 443 mW (WG1). With the modulation of a graphene absorber, pulses with a duration of 31.2 ns are produced. In particular, different laser modes can be excited in the large-cladding waveguide by adjusting the incoupling conditions, which can be promising for applications in, for example, optical vortices creation and power scaling of waveguide lasers. The double-cladding waveguide shows comparable laser performance to that of single-cladding ones even though it possesses much higher losses, suggesting great potential of such a geometry with a view to constructing efficient fiber-waveguide-fiber platforms. If the cladding pumping scheme that has been proven successful for high-power double-clad fiber lasers can be transplanted into waveguide laser technology, output power scaled up to kilowatt-level while maintaining near diffraction-limited

beam quality in the core can be expected by using double-cladding waveguides [46]. For the sake of achieving CW mode-locked waveguide lasers with high integration level and robustness, future work will involve FsLDW of integrated chirped Bragg gratings with designable dispersion in cladding waveguide lasers [47,48]. Overall, we believe this work provides an alternative approach to constructing compact and multifunctional laser sources useful for future photonic integrated circuits.

Funding

Acknowledgments

Disclosures

The authors declare no conflicts of interest.

References

1. C. Wang, M. Zhang, X. Chen, M. Bertrand, A. Shams-Ansari, S. Chandrasekhar, P. Winzer, and M. Lončar, "Integrated lithium niobate electro-optic modulators operating at CMOS-compatible voltages," Nature **562**(7725), 101–104 (2018).
2. M. He, M. Xu, Y. Ren, J. Jian, Z. Ruan, Y. Xu, S. Gao, S. Sun, X. Wen, L. Zhou, L. Liu, C. Guo, H. Chen, S. Yu, L. Liu, and X. Cai, "High-performance hybrid silicon and lithium niobate Mach-Zehnder modulators for 100 Gbit s^{-1} and beyond," Nat. Photonics **13**(5), 359–364 (2019).
3. R. Luo, Y. He, H. Liang, M. Li, and Q. Lin, "Highly tunable efficient second-harmonic generation in a lithium niobate nanophotonic waveguide," Optica **5**(8), 1006–1011 (2018).
4. A. Boes, B. Corcoran, L. Chang, J. Bowers, and A. Mitchell, "Status and potential of lithium niobate on insulator (LNOI) for photonic integrated circuits," Laser Photonics Rev. **12**(4), 1700256 (2018).
5. M.K. Bhaskar, D. D. Sukachev, A. Sipahigil, R. E. Evans, M. J. Burek, C. T. Nguyen, L. J. Rogers, P. Siyushev, M. H. Metsch, H. Park, F. Jelezko, M. Lončar, and M. D. Lukin, "Quantum nonlinear optics with a germanium-vacancy color center in a nanoscale diamond waveguide," Phys. Rev. Lett. **118**(22), 223603 (2017).
6. A. Sipahigil, R. E. Evans, D. D. Sukachev, M. J. Burek, J. Borregaard, M. K. Bhaskar, C. T. Nguyen, J. L. Pacheco, H. A. Atikian, C. Meuwly, R. M. Camacho, F. Jelezko, E. Bielejec, H. Park, M. Lončar, and M. D. Lukin, "An integrated diamond nanophotonics platform for quantum-optical networks," Science **354**(6314), 847–850 (2016).
7. C. Grivas, "Optically pumped planar waveguide lasers, Part I: Fundamentals and fabrication techniques," Prog. Quantum Electron. **35**(6), 159–239 (2011).
8. C. Grivas, "Optically pumped planar waveguide lasers: Part II: Gain media, laser systems, and applications," Prog. Quantum Electron. **45-46**, 3–160 (2016).
9. D. P. Shepherd, A. Choudhary, A. A. Lagatsky, P. Kannan, S. J. Beecher, R. W. Eason, J. I. Mackenzie, X. Feng, W. Sibbett, and C. T. A. Brown, "Ultrafast high-repetition-rate waveguide lasers," IEEE J. Sel. Top. Quantum Electron. **22**(2), 16–24 (2016).
10. Y. Jia and F. Chen, "Compact solid-state waveguide lasers operating in the pulsed regime: a review," Chin. Opt. Lett. **17**(1), 012302 (2019).
11. G. Li, N. Bai, N. Zhao, and C. Xia, "Space-division multiplexing: the next frontier in optical communication," Adv. Opt. Photonics **6**(4), 413–487 (2014).
12. S. Gross, N. Riesen, J. D. Love, and M. J. Withford, "Three dimensional ultra-broadband integrated tapered mode multiplexers," Laser Photonics Rev. **8**(5), L81–L85 (2014).
13. N. Bozinovic, Y. Yue, Y. Ren, M. Tur, P. Kristensen, H. Huang, A. E. Willner, and S. Ramachandran, "Terabitscale orbital angular momentum mode division multiplexing in fibers," Science **340**(6140), 1545–1548 (2013).
14. N. Bozinovic, S. Golowich, P. Kristensen, and S. Ramachandran, "Control of orbital angular momentum of light with optical fibers," Opt. Lett. **37**(13), 2451–2453 (2012).
15. A. Li, Y. Wang, Q. Hu, and W. Shieh, "Few-mode fiber based optical sensors," Opt. Express **23**(2), 1139–1150 (2015).
16. Y. Weng, E. Ip, Z. Pan, and T. Wang, "Single-end simultaneous temperature and strain sensing techniques based on Brillouin optical time domain reflectometry in few-mode fibers," Opt. Express **23**(7), 9024–9039 (2015).
17. G. Molina-Terriza, J. P. Torres, and L. Torner, "Twisted photons," Nat. Phys. **3**(5), 305–310 (2007).

18. A. Nicolas, L. Veissier, L. Giner, E. Giacobino, D. Maxein, and J. Laurat, "A quantum memory for orbital angular momentum photonic qubits," Nat. Photonics **8**(3), 234–238 (2014).

19. A. G. Okhrimchuk, A. V. Shestakov, I. Khrushchev, and J. Mitchell, "Depressed cladding, buried waveguide laser formed in a YAG:Nd^{3+} crystal by femtosecond laser writing," Opt. Lett. **30**(17), 2248–2250 (2005).

20. F. Chen and J. R. Vázquez de Aldana, "Optical waveguides in crystalline dielectric materials produced by femtosecond-laser micromachining," Laser Photonics Rev. **8**(2), 251–275 (2014).

21. S. Gross and M. Withford, "Ultrafast-laser-inscribed 3D integrated photonics: challenges and emerging applications," Nanophotonics **4**(3), 332–352 (2015).

22. E. Kifle, P. Loiko, J. R. Vázquez de Aldana, C. Romero, A. Ródenas, V. Zakharov, A. Veniaminov, H. Yu, H. Zhang, Y. Chen, M. Aguiló, F. Díaz, U. Griebner, V. Petrov, and X. Mateos, "Fs-laser-written thulium waveguide lasers Q-switched by graphene and MoS$_2$," Opt. Express **27**(6), 8745–8755 (2019).

23. F. Piantedosi, G. Y. Chen, T. M. Monro, and D. G. Lancaster, "Widely tunable, high slope efficiency waveguide lasers in a Yb-doped glass chip operating at 1 μm," Opt. Lett. **43**(8), 1902–1905 (2018).

24. C. Guerra-Olvera, G. R. Castillo, E. H. Penilla, G. Uahengo, J. E. Garay, and S. Camacho-Lopez, "Circular depressed cladding waveguides in mechanically robust, biocompatible nc-YSZ transparent ceramics by fs laser pulses," J. Lightwave Technol. **37**(13), 3119–3126 (2019).

25. H. Liu, Y. Tan, J. R. Vázquez de Aldana, and F. Chen, "Efficient laser emission from cladding waveguide inscribed in Nd:GdVO$_4$ crystal by direct femtosecond laser writing," Opt. Lett. **39**(15), 4553–4556 (2014).

26. M. H. Kim, T. Calmano, S. Y. Choi, B. J. Lee, I. H. Baek, K. J. Ahn, D.-I. Yeom, C. Kränkel, and F. Rotermund, "Monolayer graphene coated Yb:YAG channel waveguides for Q-switched laser operation," Opt. Mater. Express **6**(8), 2468–2474 (2016).

27. S. Y. Choi, T. Calmano, F. Rotermund, and C. Kränkel, "2-GHz carbon nanotube mode-locked Yb:YAG channel waveguide laser," Opt. Express **26**(5), 5140–5145 (2018).

28. W. Bolaños, J. J. Carvajal, X. Mateos, G. S. Murugan, A. Z. Subramanian, J. S. Wilkinson, E. Cantelar, D. Jaque, G. Lifante, M. Aguiló, and F. Díaz, "Mirrorless buried waveguide laser in monoclinic double tungstates fabricated by a novel combination of ion milling and liquid phase epitaxy," Opt. Express **18**(26), 26937–26945 (2010).

29. K. van Dalfsen, S. Aravazhi, C. Grivas, S. M. García-Blanco, and M. Pollnau, "Thulium channel waveguide laser in a monoclinic double tungstate with 70% slope efficiency," Opt. Lett. **37**(5), 887–889 (2012).

30. J. M. de Mendívil, J. del Hoyo, J. Solís, M. C. Pujol, M. Aguiló, F. Díaz, and G. Lifante, "Mirrorless Yb^{3+}-doped monoclinic double tungstate waveguide laser combining liquid phase epitaxy and multiplexed beam fs laser writing," J. Lightwave Technol. **33**(23), 4726–4730 (2015).

31. Y. F. Chen, Y. C. Liu, Y. Y. Pan, D. Y. Gu, H. P. Cheng, C. H. Tsou, and H. C. Liang, "Efficient high-power dual-wavelength lime-green Nd:YVO$_4$ lasers," Opt. Lett. **44**(6), 1323–1326 (2019).

32. Y. F. Chen, Y. Y. Pan, Y. C. Liu, H. P. Cheng, C. H. Tsou, and H. C. Liang, "Efficient high-power continuous-wave lasers at green-lime-yellow wavelengths by using a Nd:YVO$_4$ self-Raman crystal," Opt. Express **27**(3), 2029–2035 (2019).

33. Y. Jia, F. Chen, and J. R. Vázquez de Aldana, "Efficient continuous-wave laser operation at 1064 nm in Nd:YVO$_4$ cladding waveguides produced by femtosecond laser inscription," Opt. Express **20**(15), 16801–16806 (2012).

34. N. Pavel, G. Salamu, F. Jipa, and M. Zamfirescu, "Diode-laser pumping into the emitting level for efficient lasing of depressed cladding waveguides realized in Nd:YVO$_4$ by the direct femtosecondlaser writing technique," Opt. Express **22**(19), 23057–23065 (2014).

35. W. Nie, R. Li, C. Cheng, Y. Chen, Q. Lu, C. Romero, J. R. Vázquez de Aldana, X. Hao, and F. Chen, "Room-temperature subnanosecond waveguide lasers in Nd:YVO$_4$ Q-switched by phase-change VO$_2$: A comparison with 2D materials," Sci. Rep. **7**(1), 46162 (2017).

36. Z. Li, C. Cheng, N. Dong, C. Romero, Q. Lu, J. Wang, J. R. Vázquez de Aldana, Y. Tan, and F. Chen, "Q-switching of waveguide lasers based on graphene/WS$_2$ van der Waals heterostructure," Photonics Res. **5**(5), 406–410 (2017).

37. Z. Li, N. Dong, Y. Zhang, J. Wang, H. Yu, and F. Chen, "Mode-locked waveguide lasers modulated by rhenium diselenide as a new saturable absorber," APL Photonics **3**(8), 080802 (2018).

38. Z. Li, Y. Zhang, C. Cheng, H. Yu, and F. Chen, "6.5 GHz Q-switched mode-locked waveguide lasers based on two-dimensional materials as saturable absorbers," Opt. Express **26**(9), 11321–11330 (2018).

39. Y. Jia, J. R. Vázquez de Aldana, and F. Chen, "Efficient waveguide lasers in femtosecond laser inscribed double-cladding waveguides of Yb:YAG ceramics," Opt. Mater. Express **3**(5), 645–650 (2013).

40. Y. Tan, Q. Luan, F. Liu, F. Chen, and J. R. Vázquez de Aldana, "Q-switched pulse laser generation from double-cladding Nd:YAG ceramics waveguides," Opt. Express **21**(16), 18963–18968 (2013).

41. H. Liu, F. Chen, J. R. Vázquez de Aldana, and D. Jaque, "Femtosecond-laser inscribed double-cladding waveguides in Nd:YAG crystal: a promising prototype for integrated lasers," Opt. Lett. **38**(17), 3294–3297 (2013).

42. J. A. Buck, *Fundamentals of Optical Fibers* (John Wiley & Sons, 2004).

43. W. Koechner, *Solid-State Laser Engineering* (Springer, 2006).

44. J. A. Caird, S. A. Payne, P. R. Staber, A. J. Ramponi, L. L. Chase, and W. F. Krupke, "Quantum electronic properties of the Na$_3$Ga$_2$Li$_3$F$_{12}$:Cr^{3+} laser," IEEE J. Quantum Electron. **24**(6), 1077–1099 (1988).

45. A. S. Yasukevich, P. Loiko, N. V. Gusakova, J. M. Serres, X. Mateos, K. V. Yumashev, N. V. Kuleshov, V. Petrov, U. Griebner, M. Aguiló, and F. Díaz, "Modelling of graphene Q-switched Tm lasers," Opt. Commun. **389**, 15–22 (2017).

46. J. Nilsson and D. N. Payne, "High-power fiber lasers," Science **332**(6032), 921–922 (2011).

47. G. Bharathan, T. T. Fernandez, M. Ams, R. I. Woodward, D. D. Hudson, and A. Fuerbach, "Optimized laser-written ZBLAN fiber Bragg gratings with high reflectivity and low loss," Opt. Lett. **44**(2), 423–426 (2019).

48. G. Bharathan, D. D. Hudson, R. I. Woodward, S. D. Jackson, and A. Fuerbach, "In-fiber polarizer based on a 45-degree tilted fluoride fiber Bragg grating for mid-infrared fiber laser technology," OSA Continuum **1**(1), 56–63 (2018).